Taylor & Francis
Taylor & Francis Group

Coherent vortex extraction and simulation of 2D isotropic turbulence

KAI SCHNEIDER*†, MARIE FARGE‡, ALEXANDRE AZZALINI‡ and JÖRG ZIUBER§

†MSNM-CNRS & CMI, Université de Provence, 39 rue Frédéric Joliot-Curie, 13453 Marseille cedex 13, France
‡LMD-CNRS, Ecole Normale Supérieure, 24 rue Lhomond, 75231 Paris cedex 05, France
§ICT, Universität Karlsruhe, Kaiserstrasse 12, 76128 Karlsruhe, Germany

We present a method to extract coherent vortices out of turbulent flows, based on thresholding the wavelet coefficients of vorticity. We compare two ways of choosing the threshold and show how one can thus split each flow realization into coherent vortices and quasi-Gaussian white noise. We then describe a new method, called CVS (coherent vortex simulation), for computing deterministically the time evolution of the coherent vortices while neglecting or modelling the incoherent background noise. We develop a hierarchy of model equations based on the nonlinear Galerkin approach. In the first CVS method there is no modelling of the effect of the discarded coefficients and filtering out the incoherent background at each time step plays the role of turbulent dissipation. For the second approach we derive an additional linear equation to compute the effect of the incoherent background flow whose coefficients have been discarded. Finally, to validate both CVS approaches, we analyse the different terms of the filtered equations and present different simulations of homogeneous isotropic turbulence.

Keywords: computational fluid dynamics; turbulence modelling; coherent vortices; coherent vortex simulation; wavelets; turbulence

1. Introduction

Turbulence is characterized by its multiscale behaviour, self-organization into coherent structures and a generic randomness. The number of active spatial and temporal scales involved is increasing with the Reynolds number which implies a prohibitive complexity for direct approaches to compute turbulent flows. However, observations show that for a given flow realization these scales are not homogeneously distributed, neither in space nor in time, which corresponds to the flow intermittency. To be able to benefit from this property, a suitable representation of the flow should reflect the lacunarity of the fine-scale activity, in both space and time.

A prominent tool for multiscale decompositions is wavelets. A wavelet is a well-localized oscillating smooth function, i.e. a wave packet, introduced by Grossmann and Morlet [17], as basis blocks to decompose any signal or field. The wavelet is dilated to generate different scales, and translated to generate different positions and the wavelet basis functions are thus generated by the affine group. Therewith a flow field can be decomposed into scale–space contributions from which it can be perfectly reconstructed. Note that for finer scales the physical support of

---

the basis functions decreases. This is in contrast to the windowed Fourier transform where the Weyl–Heisenberg group generates modulated and translated basis functions whose support does not decrease with scale.

The flow intermittency is reflected in the sparsity of the wavelet representation, i.e. only a few coefficients, the strongest ones, are necessary to represent the dynamically active part of the flow. From corresponds to mathematical point of view this nonlinear approximation, where the coefficients are sorted by decreasing order and only the N strongest ones are retained. It yields a better precision than a linear approximation where a cut off scale is imposed *a priori*. The former, where the actual choice of the coefficients depends on the flow realization, is particularly attractive when the underlying flow field is of inhomogeneous regularity, i.e. for increasing intermittency. This property is reflected by the fact that the flow field regularity, estimated in function spaces measuring local properties of the field like Besov spaces, is larger than its regularity, estimated in function spaces measuring global properties like Sobolev spaces.

Note that Besov spaces are used indirectly in the turbulence community since the Besov norms are equivalent to the structure functions, see e.g. [28]. This nonlinear approximation allows efficient and sparse representations of such functions with inhomogeneous regularity using few coefficients nevertheless preserving excellent precision. These properties have been proven by DeVore and co-workers [7] and are well known in the approximation theory community.

A second ingredient in turbulent flows is that the observed coherent structures seem to be imbedded in a random background sea. In statistics wavelets have turned out to be a suitable tool for this denoising task [9, 8]. It has been proven rigorously that wavelet thresholding of noisy data allows us to estimate the underlying signal, given its inhomogeneous regularity, in a quasi-optimal way. This is due to the sparsity of the wavelet representation of the signal and the property that noise is invariant under orthogonal transformations, which means that a noise remains a noise in any basis and does not become sparse.

Wavelet techniques have been introduced in the early nineties to analyse turbulent flows [10, 21]. Since then different directions for wavelets and turbulence have been pursued, e.g. signal processing approaches, interpretations in the multifractal community, co-spectra, analyses and eduction of coherent structures using experimental data.

In [11, 12] we have introduced the coherent vortex simulation (CVS) approach to compute and model turbulent flows. Further developments have been presented in [14, 18]. The idea of CVS is to combine nonlinear approximation with denoising and additionally to exploit the properties of wavelets for numerical analysis. Wavelets yield attractive discretizations for operator equations. They allow auto-adaptive discretizations by estimating the local regularity of the solution. Furthermore, many integral and differential operators have a sparse representation in a wavelet basis and can furthermore efficiently be preconditioned using diagonal scaling. For a review we refer to the book of Cohen [4]. The idea of CVS is based on filtering turbulent flows using adaptive multiresolution techniques. Therewith the flow is split into two parts, a coherent flow, whose evolution is deterministically computed in an adaptive basis, and an incoherent flow, which is noiselike and whose effect on the coherent flow is modelled.

The aim of the present paper is to present CVS in a concise way by combining the aspect of nonlinear approximation and denoising first for the extraction of coherent vortices. We assess the iterative wavelet-based denoising algorithm, which was justified mathematically in [1], for extracting vortices in two-dimensional flows. We also show that this scheme can be interpreted as a nonlinear diffusion process. Then we present the previously introduced CVS approach [11, 12] and derive a hierarchy of model equations, taking into account the influence of the incoherent part of the flow. Different numerical simulations of two-dimensional turbulent flows show the validity of the CVS models. Finally, we conclude and present some perspectives for 3D flows.

2. Wavelet-based coherent vortex extraction

2.1 *Orthogonal wavelets and denoising*

In the following we fix the notation for the wavelet decomposition of a one-dimensional scalar valued signal and summarize the main ideas of wavelet-based denoising. For more details on the orthogonal wavelet transform, its extension to higher dimensions, we refer the reader to textbooks, e.g. [6].

We consider a signal u and decompose it into an orthogonal wavelet series

$$u(x) = \sum_{\lambda \in \Lambda} \widetilde{u}_\lambda \psi_\lambda(x), \tag{1}$$

where the multi-index $\lambda = (j, i)$ denotes the scale j and the position i of the wavelets. The corresponding index set Λ is $\Lambda = \{\lambda = (j, i), j = 0 \ldots, i = 0 \ldots 2^j - 1\}$. Due to orthogonality the coefficients are given $\widetilde{u}_\lambda = \langle u, \psi_\lambda \rangle$ where $\langle \cdot, \cdot \rangle$ denotes the L^2-inner product.

When a signal s is corrupted by Gaussian white noise n, i.e. we observe $u = s + n$, then this noise is contained to a small amount in all wavelet coefficients $\widetilde{u}_\lambda$, while the original signal s is in general determined by few significant coefficients. The idea of wavelet denoising can be summarized in the following three-step procedure:

- *Decomposition:* compute the wavelet coefficients $\widetilde{u}_\lambda$ using the fast wavelet transform.
- *Thresholding:* apply the thresholding function ρ_ε to the wavelet coefficients $\widetilde{u}_\lambda$, thus reducing the relative importance of the coefficients with small absolute value.
- *Reconstruction:* reconstruct a denoised version u_C from the thresholded wavelet coefficients using the fast inverse wavelet transform.

The thresholding parameter ε depends on the variance of the noise and on the sample size. Different thresholding functions ρ are used in the statistical community, the most prominent ones are linear, soft, hard and firm thresholding.

In the following we consider hard thresholding corresponding to

$$\rho_\varepsilon(a) = \begin{cases} a & \text{if } |a| > \varepsilon \\ 0 & \text{if } |a| \leq \varepsilon \end{cases}, \tag{2}$$

where ε denotes the threshold.

For soft and hard thresholding Donoho and Johnstone have shown [9] that the relative quadratic error between the signal s and its estimator u_C is close to the minimax error for all signals $s \in \mathcal{H}$, where $\mathcal{H}$ belongs to a wide class of function spaces, including Hölder and Besov spaces. They also showed using the threshold

$$\varepsilon_D = \sigma_n \sqrt{2 \ln N} \tag{3}$$

yields an error which is close to the minimum error. Since ε_D depends only on the number of samples N and on the variance of the noise σ_n^2, it is called universal threshold. However, in many applications σ_n^2 is unknown, like in turbulence, and has to be estimated from the available noisy data u. In [1] we have developed an iterative algorithm for this task, based on the method presented in [11], which is briefly sketched in the following.

Initialization

- given $u_k, k = 0, \ldots, N - 1$. Set $i = 0$ and compute the fast wavelet transform of u to obtain $\widetilde{u}_\lambda$.

- compute the variance σ_0^2 of u as a rough estimate of the variance of n and compute the corresponding threshold $\varepsilon_0 = (2 \ln N \sigma_0^2)^{1/2}$.
- set the number of coefficients considered as noise $N_{\text{noise}} = N$.

Main loop

Repeat

- set $N'_{\text{noise}} = N_{\text{noise}}$ and count the wavelet coefficients N_{noise} with modulus smaller than ε_i.
- compute the new variance σ_{i+1}^2 from the wavelet coefficients whose modulus is smaller than ε_i and the new threshold $\varepsilon_{i+1} = (2(\ln N)\sigma_{i+1}^2)^{1/2}$.
- set $i = i + 1$

until $(N'_{\text{noise}}{==}N_{\text{noise}})$.

Final step

- compute u_C from the coefficients with modulus larger than ε_i using the inverse fast wavelet transform.

In [1] we have proven that the algorithm converges within a finite number of iterations which is in practice small. The iterations are performed in wavelet coefficient space and hence the algorithm only requires one fast wavelet transform and one inverse which are both of $\mathcal{O}(N)$.

2.2 *Coherent vortex extraction algorithm*

In [11, 13], a wavelet-based method to extract coherent vortices out of both two- and three-dimensional turbulent flows was proposed. The idea is to apply the previously described denoising algorithm to the vorticity field ω given at resolution N at a given time instant t. Therewith the flow is split into two parts: a coherent flow corresponding to the coherent vortices and an incoherent flow corresponding to the noise [11].

This decomposition yields $\omega = \omega_C + \omega_I$. Due to orthogonality we have $\langle \omega_C, \omega_I \rangle = 0$ and hence it follows that enstrophy is conserved, i.e. $Z = Z_C + Z_I$.

Inverting the curl operator we obtain the corresponding velocity fields, i.e. $\vec{v} = \vec{v}_C + \vec{v}_I$. As the Biot–Savart operator is not diagonal in wavelet space we have for the energy that $E = E_C + E_I + \epsilon$ where ϵ is small (cf. [11]).

2.3 *Application to 2D turbulence*

In the following we apply the coherent vortex extraction algorithm to a 2D turbulent vorticity field (figure 1) computed by direct numerical simulation at resolution 512^2 using a classical Fourier pseudo-spectral method [2]. Note that for this computation hyperviscosity was used.

We compare two cases: in the first we use the threshold ε_0, based on the variance of the enstrophy of the total flow, and in the second we apply the iterative scheme to compute the threshold ε_{it}. Using the threshold ε_0, we find that $C = 0.32\%$ of the modes are retained in the coherent contribution which contain 82.31% of the variance of the vorticity. Using ε_{it} gives a weaker compression ratio, with 3.22% of the modes retaining 95.44% of the enstrophy. We observe that filtering with ε_0 does not preserve the isotropy of the coherent vortices (figure 2). Moreover, considering 1D cuts of the incoherent field in figure 2, we observe that still some vortices can be found. In contrast, the isotropy of the vortices is perfectly respected using ε_{it} and all vortices have been removed from the incoherent background flow. This fact is confirmed when we look at the PDFs of the vorticity (figure 3) since we have a Gaussian distribution
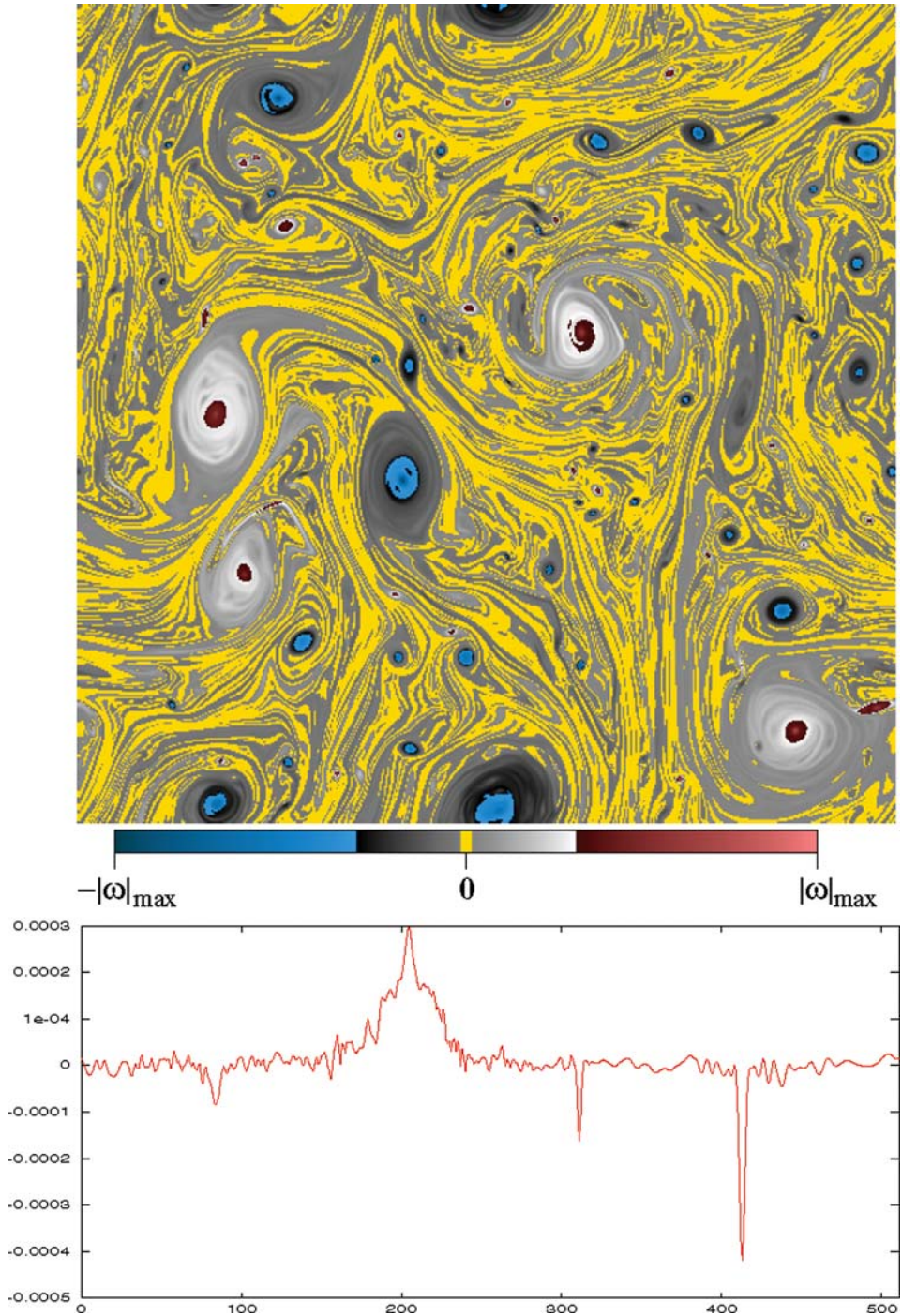
Figure 1. Two-dimensional turbulent vorticity field and horizontal cut.

for the incoherent background obtained when filtering with $\varepsilon_{\mathrm{it}}$, while we have a non-Gaussian distribution when using ε_0, which is due to the presence of small vortices still present in the incoherent field. Nevertheless, both filtering methods show a very good fit between the PDFs of the total and coherent fields.
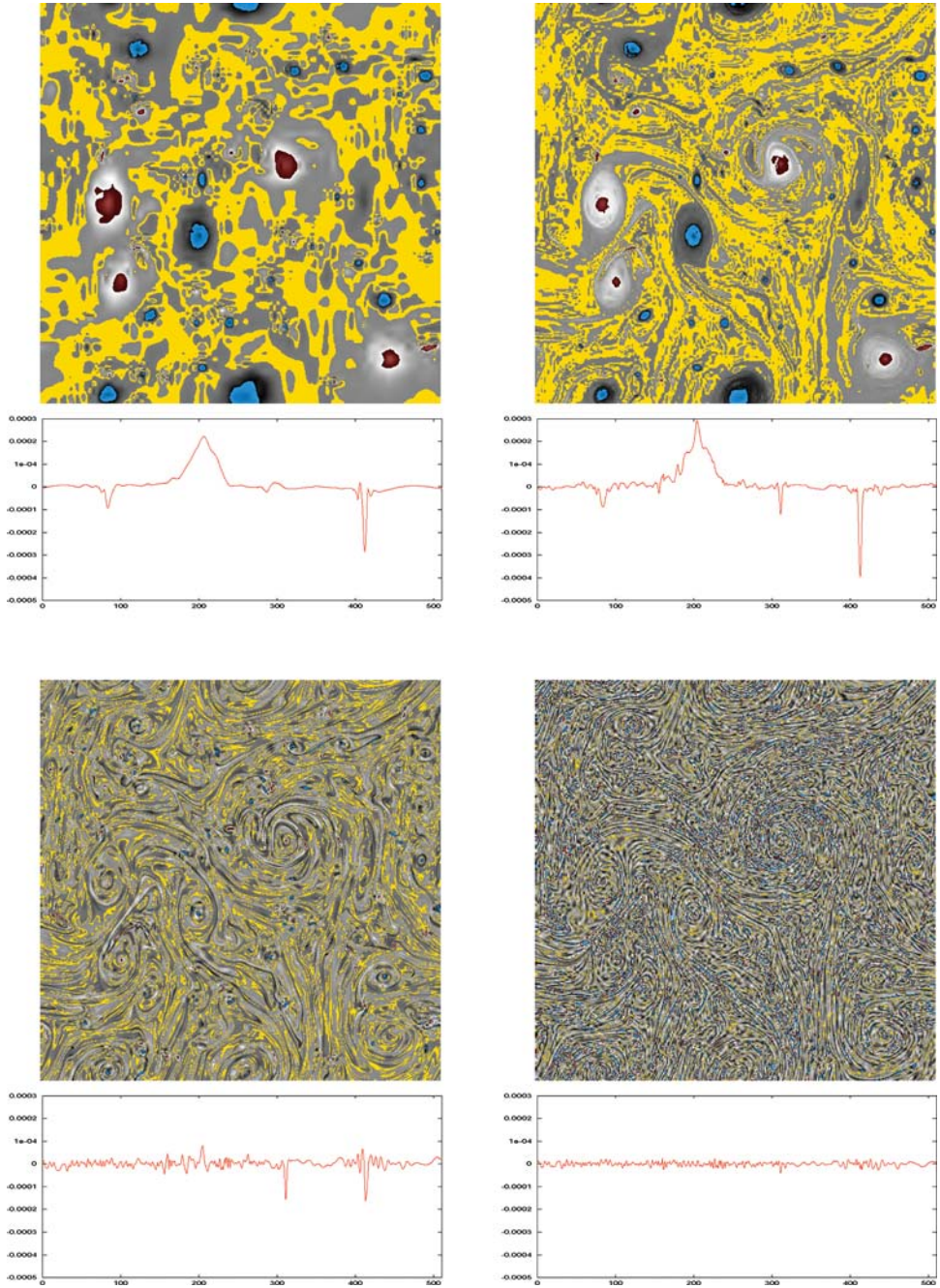
Figure 2. Coherent vortex extraction using ε_0 (left column) and ε_{it} (right column). Top row: coherent vorticity; Bottom row: incoherent vorticity.

Finally, if we consider the enstrophy spectra (figure 4), we observe that the incoherent background obtained using ε_{it} shows a tendency towards enstrophy equipartition, which corresponds to a k^{+1} scaling. Moreover, we observe that in the large scales, up to wave number $k = 30$, all the contribution to the enstrophy comes from the coherent modes. Concerning the filtering using ε_0, the behaviour of the enstrophy spectrum confirms that we did not properly
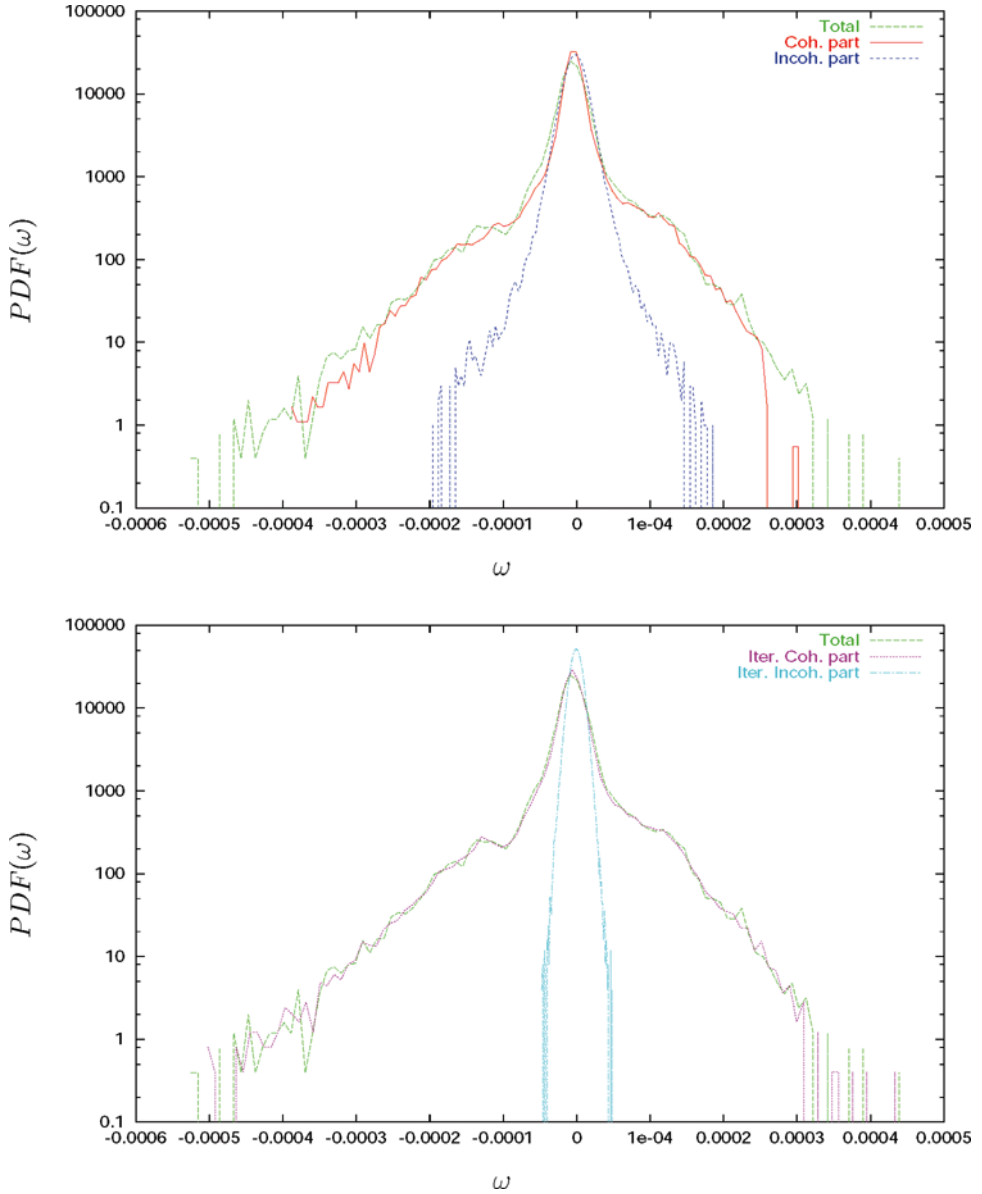
Figure 3.   Coherent vortex extraction using ε_0 (top) and ε_{it} (bottom). PDFs of the total, coherent and incoherent vorticity.

separate coherent and incoherent contributions, since the coherent and total enstrophy spectra begin to depart for scales smaller than wave number $k \simeq 10$. The incoherent enstrophy does not present the same equipartition as we have obtained using ε_{it}.

2.4   *Coherent vortex extraction and nonlinear diffusion*

The extraction of coherent vortices using nonlinear wavelet thresholding can be interpreted as the application of a nonlinear diffusion operator to the vorticity field. Nonlinear diffusion is
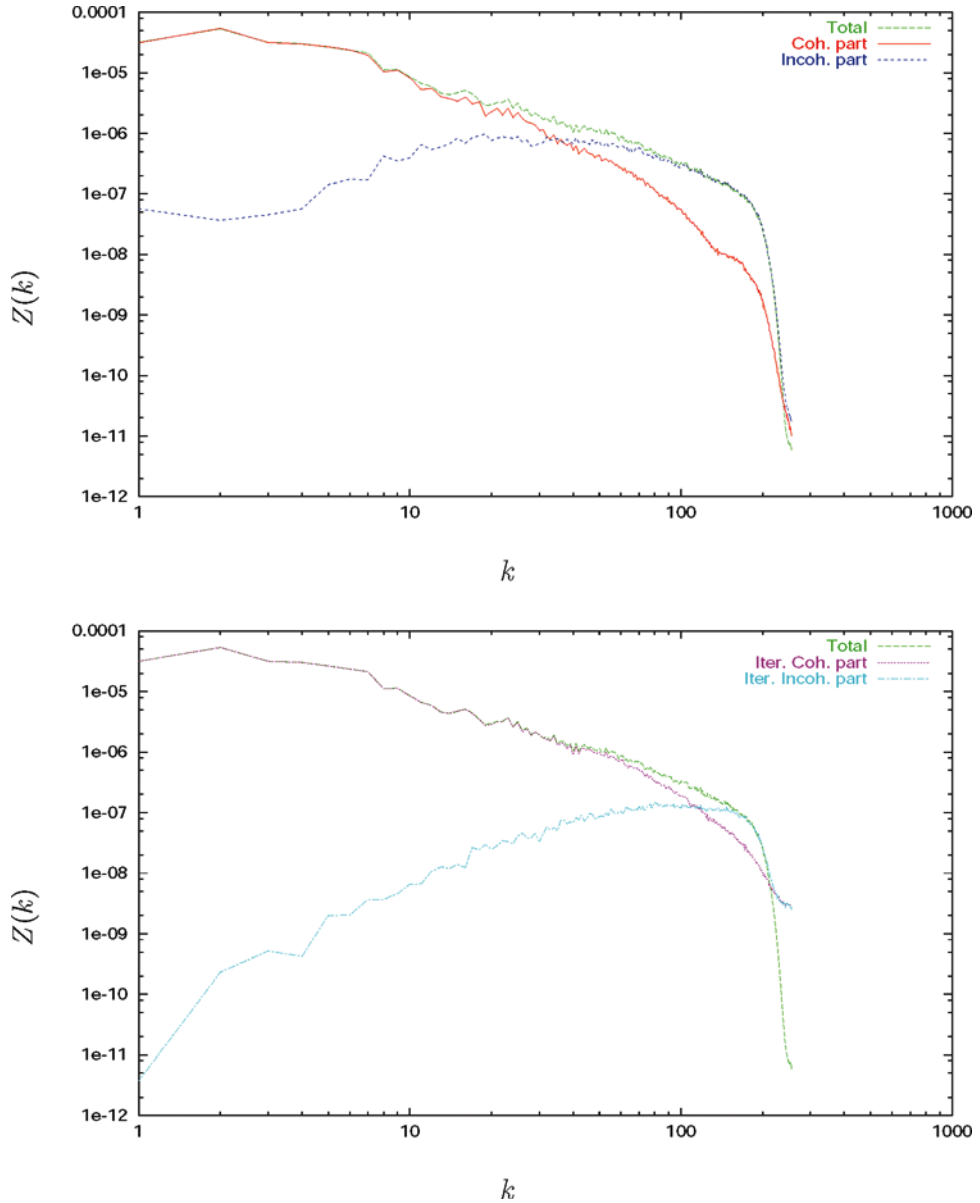
Figure 4.   Coherent vortex extraction using ε_0 (top) and ε_{it} (bottom). Enstrophy spectra of the total, coherent and incoherent vorticity.

used in image processing to restore images from noisy data [23]. We briefly sketch the main ideas. Starting from a noisy image u_0 and evolving it in time according to a process described by a nonlinear PDE,

$$\partial_t u = \nabla \cdot (\nu(|\nabla u|) \nabla u) \tag{4}$$

with initial condition $u(x, t = 0) = u_0(x)$, one obtains a denoised image. The diffusivity function ν depends on the modulus of the signal gradient. It is non-negative and decaying for increasing magnitude of the signal gradient. The result is that smoothing is faster in

homogeneous regions, where the gradient is small and fine-scale contributions are caused by the noise. Regions of large gradients, e.g. discontinuities, which correspond to important features of the image, are preserved due to small diffusion there.

In [22] the equivalence between nonlinear wavelet thresholding (using Haar wavelets) and a single step of explicitly discretized nonlinear diffusion using centred finite differences has been shown. For hard thresholding the diffusion coefficient ν corresponds to

$$\nu(x) = \begin{cases} \dfrac{1}{4\tau} & \text{if } |x| \leq \sqrt{2}\varepsilon, \\ 0 & \text{if } |x| > \sqrt{2}\varepsilon \end{cases}, \tag{5}$$

where $\varepsilon = \sqrt{2}\tau$ and τ denotes the time step size.

This relation between wavelet thresholding and nonlinear diffusion shows that the extraction of coherent vortices can be seen as the application of nonlinear diffusion to the total vorticity field. The proposed discarding of the influence of the incoherent part in the CVS computation of the flow evolution to model turbulent dissipation can therewith be justified.

3. Principle of coherent vortex simulation (CVS)

In this section we present the application of the previously presented coherent vortex extraction technique to turbulent flow simulations, performing coherent vortex simulations [11]. For the statistical analysis of single turbulent flow fields, it has been demonstrated in section 2.3 that wavelet filtering is an efficient tool to split a turbulent flow into coherent vortices and an incoherent background flow. Although the filtered coherent flow part is highly compressed in wavelet space, it conserves most of the total energy and enstrophy of the original flow field. This property motivates the simulation of turbulent flows using only the reduced wavelet basis instead of the total number of degrees of freedom, which will finally reduce the overall computational cost.

We first develop the model equations, i.e. the CVS equations introduced in [11] and an improved model including a model equation for the evolution of the incoherent flow. Then we introduce the adaptive basis concept of CVS and explain the implementation of the basis selection.

3.1 *Development of the CVS model equations*

The starting point is the two-dimensional Navier–Stokes equations in vorticity–velocity formulation

$$\partial_t \omega + \vec{v} \cdot \nabla \omega - \nu \nabla^2 \omega = \nabla \times \vec{f} \tag{6}$$

$$\nabla \cdot \vec{v} = 0$$

$$\omega(0, \vec{x}) = \omega_0,$$

where the unknown is the scalar valued vorticity $\omega = \nabla \times \vec{v}$, with $\vec{v}$ being the velocity; $\vec{f}$ is a given forcing, and $\nu > 0$ the kinematic constant viscosity. The above equations are completed with periodic boundary conditions. The velocity can be reconstructed from the vorticity using the Biot–Savart relation,

$$\vec{v} = \nabla^\perp (\nabla^2)^{-1} \omega \tag{7}$$

with $\nabla^\perp = (-\partial y, \partial x)$.

Using the decomposition of the flow into coherent and incoherent components, i.e.

$$\omega = \omega_C + \omega_I \quad \text{and} \quad \vec{v} = \vec{v}_C + \vec{v}_I, \tag{8}$$

and projecting (6) onto coherent and incoherent components we obtain an equivalent system

$$\partial_t \omega_C + (\vec{v}_C \cdot \nabla \omega_C + \vec{v}_C \cdot \nabla \omega_I + \vec{v}_I \cdot \nabla \omega_C + \vec{v}_I \cdot \nabla \omega_I)_C - \nu \nabla^2 \omega_C = \nabla \times \vec{f}_C \tag{9}$$

$$\partial_t \omega_I + (\vec{v}_C \cdot \nabla \omega_C + \vec{v}_C \cdot \nabla \omega_I + \vec{v}_I \cdot \nabla \omega_C + \vec{v}_I \cdot \nabla \omega_I)_I - \nu \nabla^2 \omega_I = \nabla \times \vec{f}_I \tag{10}$$

$$\nabla \cdot \vec{v}_C = 0 \quad \text{and} \quad \nabla \cdot \vec{v}_I = 0$$

$$\omega_C(0, \vec{x}) = (\omega_0)_C \quad \text{and} \quad \omega_I(0, \vec{x}) = (\omega_0)_I$$

which describes the evolution of the coherent and incoherent flow and their coupling in the spirit of nonlinear Galerkin methods, see e.g. [5, 19].

For the two-dimensional Navier–Stokes equations it is well known that the global attractor of (6) is contained in the balls [5]

$$||\omega|| \leq \rho_0 \quad ||\nabla \omega|| \leq \rho_1 \quad \text{and} \quad ||\nabla^2 \omega|| \leq \rho_2, \tag{11}$$

where the radii ρ_i depend on the forcing $\vec{f}$, ν and on the initial data ω_0. The bounds are uniform and apply for all times $t \in I\!R$, since the global attractor is invariant [5]. The above estimations are used in [19] to develop error analyses of postprocessing Galerkin and nonlinear Galerkin methods. By construction similar estimates as in equation (11) hold for the coherent and incoherent flow.

In the following we derive estimations for the magnitude of the different terms. For the norm of the incoherent vorticity we have $||\omega_I|| = O(\varepsilon)$ where ε denotes the threshold [4]. Thanks to the norm equivalence of the wavelet decomposition we obtain estimates for the gradient of vorticity, $||\nabla \omega|| \cong 2^J ||\omega||$, and for the velocity $||\vec{v}|| \cong 2^{-J} ||\omega||$. This shows that the magnitude of the gradient of the incoherent vorticity increases with the resolution (and hence the Reynolds number), while the magnitude of the incoherent velocity decreases for increasing J.

This yields the following orders of magnitude of the different terms:

- $O(1)$ terms: ∇w_I and $\nabla^2 \omega_I$,
- $O(\varepsilon)$ terms: ω_I,
- $O(\varepsilon^2)$ terms: $\vec{v}_I$.

The terms for the coherent flow $(\omega_C, \nabla \omega_C, \nabla^2 \omega_C, \vec{v}_C)$ are all by construction of $O(1)$. Neglecting terms of increasing orders we obtain a hierarchy of CVS models [11, 12].

Retaining only terms containing the coherent flow we obtain the following model equations:

CVS $O(1)$

$$\partial_t \omega_C + (\vec{v}_C \cdot \nabla \omega_C)_C - \nu \nabla^2 \omega_C = \nabla \times \vec{f}_C \tag{12}$$

$$\nabla \cdot \vec{v}_C = 0$$

$$\omega_C(0, \vec{x}) = (\omega_0)_C.$$

Note that in this system the influence of the incoherent flow is completely neglected and only the time evolution of the coherent flow is computed.

Retaining the $O(1)$ and additionally the $O(\varepsilon)$ terms we obtain more complete equations:

CVS $O(\varepsilon)$

$$\partial_t \omega_C + (\vec{v}_C \cdot \nabla \omega_C + \vec{v}_C \cdot \nabla \omega_I)_C - \nu \nabla^2 \omega_C = \nabla \times \vec{f}_C \tag{13}$$

$$\partial_t \omega_I + (\vec{v}_C \cdot \nabla \omega_C + \vec{v}_C \cdot \nabla \omega_I)_I - \nu \nabla^2 \omega_I = \nabla \times \vec{f}_I \qquad (14)$$

$$\nabla \cdot \vec{v}_C = 0 \quad \text{and} \quad \nabla \cdot \vec{v}_I = 0$$

$$\omega_C(0, \vec{x}) = (\omega_0)_C \quad \text{and} \quad \omega_I(0, \vec{x}) = (\omega_0)_I.$$

We observe that the equation for ω_I is a linear advection–diffusion equation, where the coherent velocity $\vec{v}_C$ is given.

3.2 *Selection of the active degrees of freedom*

Performing numerical simulations using CVS implies the integration of the governing equations with a reduced set of degrees of freedom. This is achieved by filtering the flow represented in wavelet space at each time step, and thus selecting the active coefficients retained for the numerical integration.

We apply at each time step the denoising algorithm which only retains the coherent vortices responsible for the nonlinear dynamics which trigger the flow evolution. We first study the structure of the isosurface corresponding to the threshold value and check if it defines a simply connected manifold. Since the extraction algorithm uses orthogonal wavelets, the corresponding coefficients are only defined on a dyadic lattice indexed by discrete scales, corresponding to octaves j, and discrete positions, $(i_x/2^j, i_y/2^j)$. To be able to visualize this interface, we interpolate the orthogonal wavelet coefficients to obtain a new representation on an equidistant lattice, taking three voices s per octave to obtain 27 scales, and upsampling to 512^2 positions at each scale.

We consider the same DNS as presented in section 2.3. In the movie, figure 5, we show the time evolution of the vorticity field starting from a random initial condition and integrated during 30 eddy turnover times without forcing.
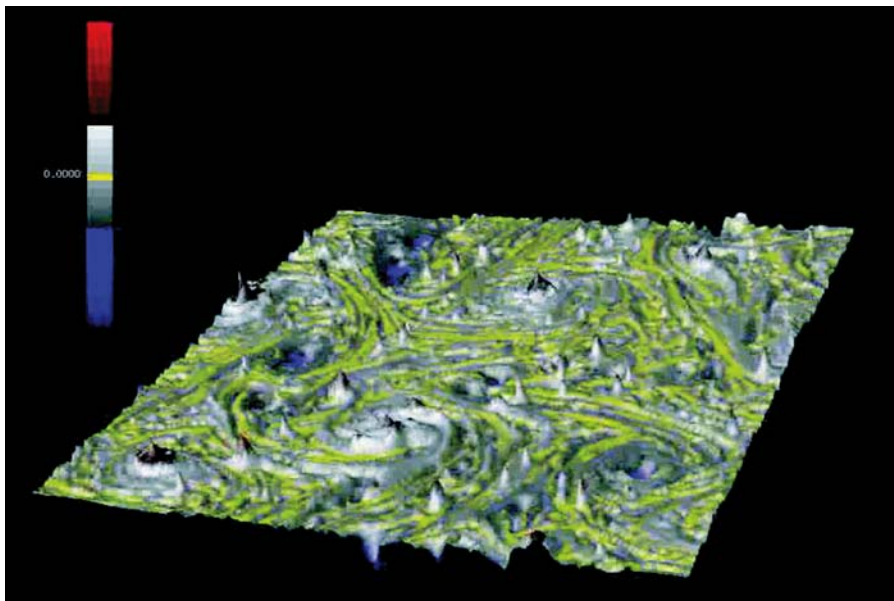
Figure 5.   Perspective view of the vorticity field at a given instant.

Figure 6.   Perspective view of the vorticity field at a given instant. Superimposed is a cut in the wavelet coefficient space. The red curve corresponds to the threshold value which defines the interface in wavelet space between coherent and incoherent flow.

In the movie, figure 6, we show the vorticity field at a given instant, together with a plane corresponding to a vertical cut of the wavelet coefficient space. This plane shows the enstrophy distribution in one direction of space (horizontal axis) and scale (vertical axis). The time evolution, i.e. the plane moving from back to the front, scans the other space direction. The colour scale corresponds to the enstrophy value of the wavelet coefficients represented in space and scale. The red isoline corresponds to the threshold value which defines the interface in wavelet space between the coherent and incoherent flow. We observe that this curve is most of the time continuous and thus splits the wavelet coefficients into two simply connected domains. From time to time, there are some disconnected parts but they remain in the vicinity of the interface. In the next section we will introduce a so-called security zone which will reconnect these regions.

In the movie, figure 7, we show the time evolution of the manifold, corresponding to the isosurface of the wavelet coefficients whose magnitude is equal to the threshold value. This interface thus splits the flow dynamics into two separated regions:

- The portion of wavelet space above this manifold contains the wavelet coefficients weaker than the threshold which correspond to the noise associated with the linear dissipation term of Navier–Stokes equations.
- The portion of wavelet space below this manifold contains the wavelet coefficients larger than the threshold which correspond to the coherent vortices associated with the nonlinear advection term of Navier–Stokes equations.

The movie illustrates the stability of the coherent vortices seen from the wavelet coefficient space. It also confirms that this manifold remains continuous, which will allow us to retain only as active degrees of freedom the coefficients below the manifold, plus the nearest coefficients above defining the security zone, as explained below.
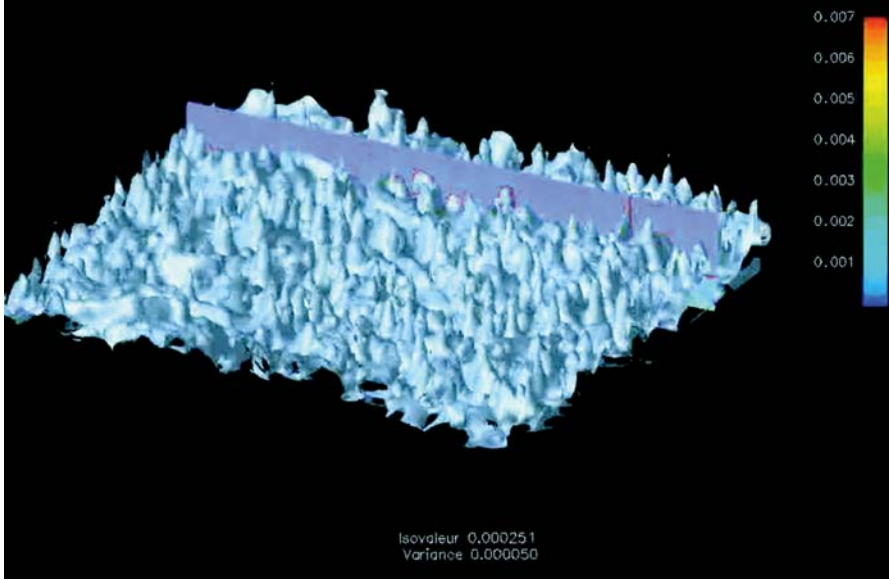
Figure 7. Visualization in the wavelet coefficient space of the interface between coherent and incoherent flow at a given instant.

3.3 *Addition of a security zone in wavelet space*

The previous movies, figures 6 and 7, show that the interface delimiting the set of active degrees of freedom, corresponding to the coherent vortices, evolves in time. To compute the flow evolution with a reduced number of degrees of freedom we track the position of this interface in space and scale. Knowing the interface at a given time step we have to guess its new position for the next time step. For this we add a security zone by adding the nearest wavelet coefficients in both space and scale. We then compute the solution at the next time step in this new set of coefficients, and then apply the threshold based on the vorticity field at the new time step.

The time evolution of a turbulent flow results in the movement of its structures in space and scale. With respect to the reduced integration domain this includes movements to regions that are not captured by the initially filtered wavelet basis. This effect is illustrated for an isolated one-dimensional structure in figure 8. Filtering the wavelet coefficients at a time step by applying the threshold ε, a structure, e.g. a vortex, is represented by the coefficients $|\tilde{\omega}| > \varepsilon$ (white area under the solid line curve). All coefficients $|\tilde{\omega}| \leq \varepsilon$ are neglected and their corresponding wavelets are not considered for the integration. The structure moves in space and scale within the determined integration step (indicated by the arrow) and then, it could be represented by the coefficients under the dashed lined curve. We recognize that some of these coefficients (hatched area) are not captured by the initially retained coefficients. Therefore, they would be ignored for the integration and their corresponding dynamical information is irreversibly lost. To avoid this effect, we retain for the integration basis, together with the coefficients $|\tilde{\omega}| > \varepsilon$, their local neighbours in wavelet space, which constitute the *security zone* (grey area). It is the function of the security zone to provide room for the solution to evolve in space and scale. In figure 8 it is illustrated that the movement of the structure within the determined integration step is captured by the enlarged basis and no dynamical information is lost.
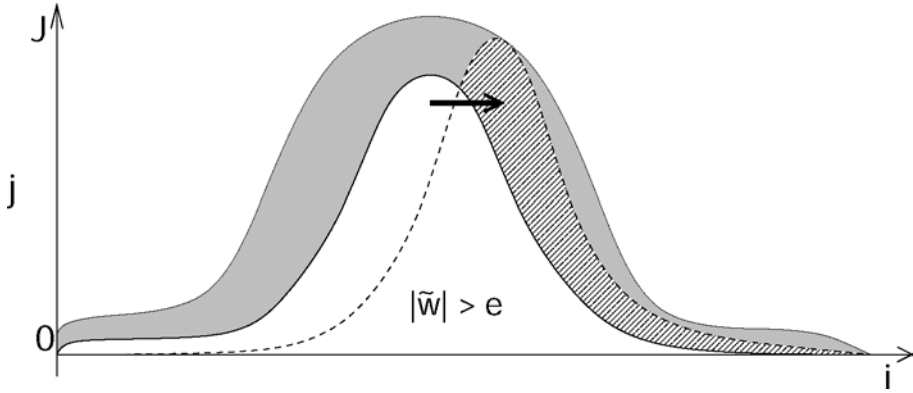
Figure 8.   Effect of the security zone extension. The wavelet coefficient space of a one-dimensional signal is shown, spanned by the scale j and the position i. After filtering with a threshold ε a structure is represented by its coefficients $|\tilde{\omega}| > \varepsilon$ in wavelet space (white area under the solid curve). By integrating the governing equations, the structure moves in space and scale and then is represented by the coefficients under the dotted lined curve. The security zone (grey domain) captures both sets of coefficients.

It is obvious that the set of filtered wavelet coefficients extended by the security zone reduces compression. The challenge is to find a minimal security zone capturing all degrees of freedom necessary to catch the flow dynamics. The security zones chosen for the two-dimensional simulations are presented in the following.

3.3.1   Security zone in two dimensions.   Figure 9 illustrates the selection of the security zone in two dimensions. For each coefficient, fulfilling the threshold filtering condition $|\tilde{\omega}| > \varepsilon$, the coefficient itself ($\bullet$) and automatically all its neighbours ($\times$) are retained in the filtering procedure. This neighbourhood includes coefficients on the same scale (light grey) as
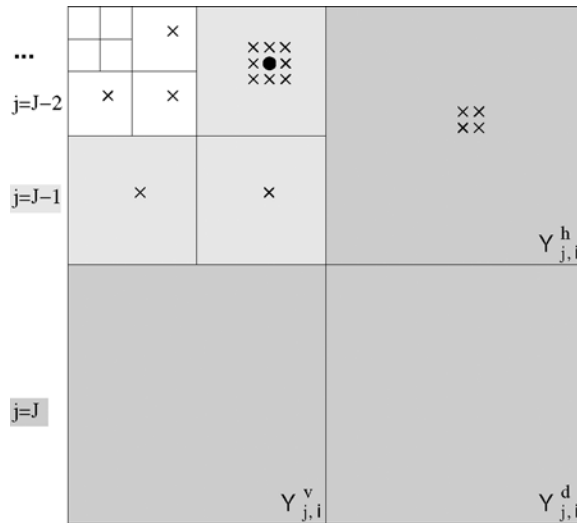
Figure 9.   Example for the selection of the security zone in two-dimensional wavelet space. For every scale j each of the three quarters represents 2^{2j} coefficients corresponding to the wavelets $\Psi^{\mu=h,v,d}_{j,i}$ oriented in horizontal (h), vertical (v) and diagonal (d) directions, respectively (cf. [6]). When the absolute value of the coefficient at position $\bullet$ is larger than the threshold, then the coefficient itself and automatically all its neighbours $\times$ are retained in the filtering procedure.

well as the corresponding coarser (dark grey) and finer (white) scales. Considering the nearest neighbours only is justified by the semi-implicit time integration which implies a CFL condition due to the nonlinear term. Because wavelet coefficients are localized in both scale and space we include proximity information as well locally as in phase space. The security zone presented in figure 9 is one possible choice, offering to the solver the possibility of evaluating a solution in all directions and scales. Different types of security zones are possible, affecting compression and the capability of conserving dynamical information of the filtered flow.

4.   Numerical results

In this section we present results for the application of CVS to two-dimensional turbulent flows. First, we show a direct numerical simulation of the flow evolution, representing the reference case. Considering different ways of threshold selection for wavelet filtering, we present simulations using the estimated threshold ε_0 and the iteratively evaluated threshold $\varepsilon_{it} \approx \varepsilon_D$, introduced in section 2.1. In both cases the security zone extension (cf., section 3.3.1) is applied. Two further simulations are shown to illustrate the effect and necessity of the security zone imposing the same compression rate, one with and the other without it. We analyse the compression properties of each method as well as its capability of conserving the dynamics of the flow during the simulation.

4.1   *DNS reference run*

As reference simulation we compute by DNS a decaying homogeneous isotropic flow with Newtonian viscosity using a classical Fourier pseudo-spectral method [2]. The equations are normalized by the initial r.m.s. velocity v_0 and vorticity ω_0, and the computational domain length L_0. For the presented simulations the forcing term f is set to zero, i.e. the flow decays. With the selected kinematic viscosity v the resulting initial Reynolds number for the presented flow becomes $Re = v_0 L_0 / v \approx 8722$. The equations are integrated in the domain $\Omega = [0; 1]^2$ with resolution $N = 512^2$. The given time scales are normalized with $\tau = 1/\sqrt{2Z_0}$, where Z_0 is the total enstrophy at $t = 0$.

In figure 10 the vorticity fields are depicted for the initial condition and the end of the simulation. From the vorticity plots typical behaviour of two-dimensional turbulent flows can be identified: The number of vortices decreases as a consequence of the merging of co-rotating vortices. Fine-scale structures like elongated filaments are formed by vortex interaction, i.e. local fluid elements are compressed in one direction and simultaneously stretched in another. Due to viscous dissipation the overall vorticity amplitude decreases.

The energy spectra are plotted in figure 10 (bottom). From statistical theory a k^{-3} inertial range would be expected for two-dimensional turbulence. In numerical simulations either a k^{-3} behaviour is found when starting with random initial conditions with a narrow band spectrum (see e.g. [3]) or steeper decays proportional between k^{-4} and k^{-5} are found starting with broadband random initial conditions [20]. For the presented simulation we used a broadband random initial condition and find spectra with a k^{-4}-slope, which is hence consistent with the literature. The total energy of the flow slowly decays, as no forcing is used. The shape of the spectrum remains very similar during the evolution.

4.2   *CVS of two-dimensional turbulent flows*

In section 2.3 we have seen that wavelet filtering of a turbulent flow at a given time instant preserves almost the whole energy and most of the enstrophy, coming along with a very high
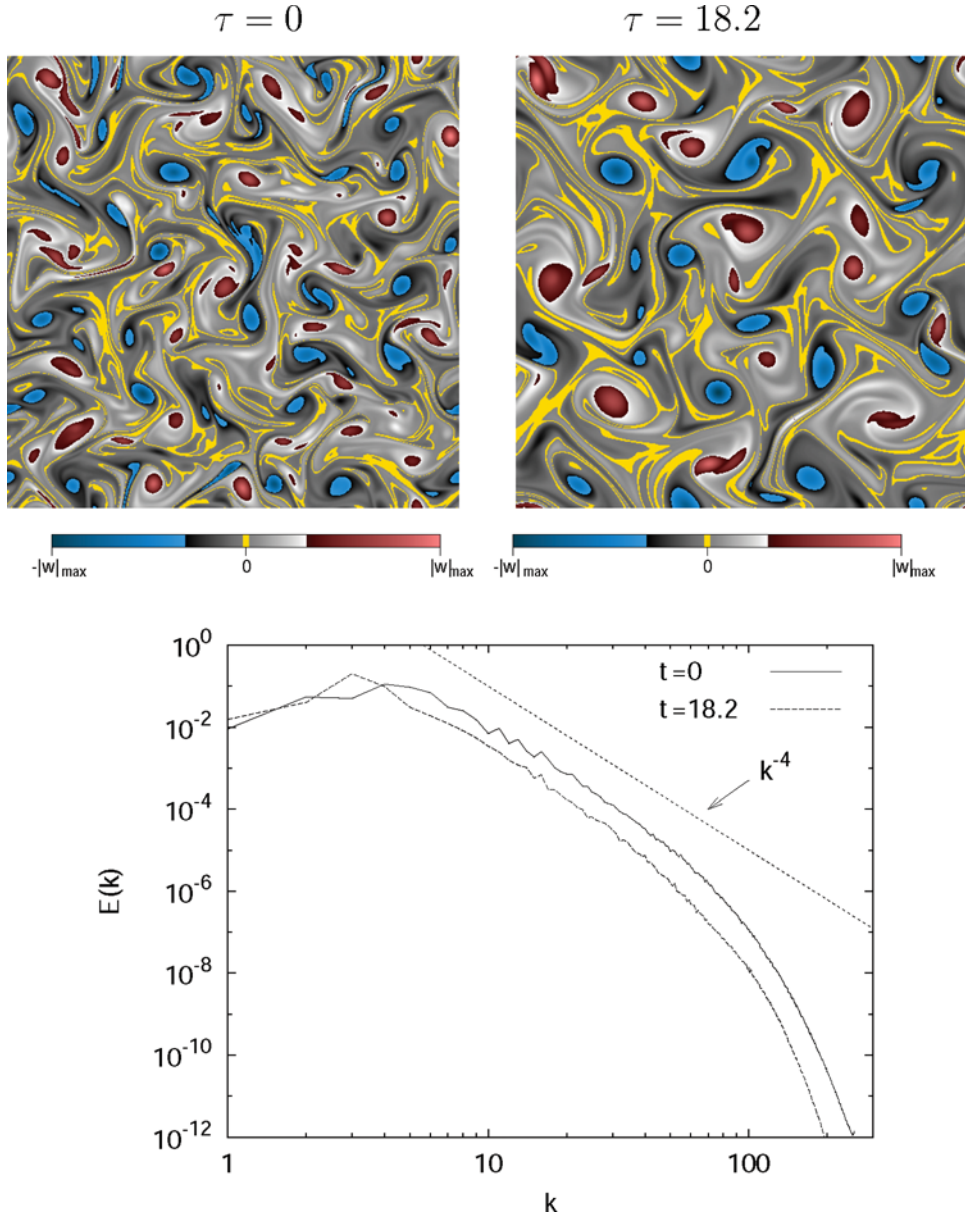
Figure 10. Direct numerical simulation (DNS) of 2d turbulence. Vorticity at $\tau = 0$, ($|\omega|_{\max} = 232.5$) and at $\tau = 18.2$ ($|\omega|_{\max} = 156.3$)(top). Corresponding energy spectra (bottom).

compression. We now check the influence of the filtering on the flow evolution and compare the CVS results with the DNS. As in the analysis section we focus on the compression properties of the presented filtered simulations as well as on their capability of preserving the flow dynamics.

Starting with the vorticity field ω at time $t = 0$ we extract the coherent vorticity ω_C. Note that the filter differs depending on the choice of the threshold, as described below. Then we perform an integration for one time step and we obtain $\omega_C^\star$. The time step is then completed by reprojecting $\omega_C^\star$ to the basis of ω_C by applying the filter again. Therewith we integrate

Table 1. Compression ratio and conservation properties of the initial conditions ($\tau = 0$) in the case of the CVS-filtered simulations compared to DNS.

Run	Compression ratio (%)	Energy (%)	Enstrophy (%)
CV-DS	46.9	100	100
CV-6	7.0	100	99.9
CV-1S	6.7	99.9	99.4
CV-TS	2.2	99.6	96.2

equation (12). In the following studies Coiflet12 wavelets are used. The simulation parameters are identical with those of the DNS run.

To study two general aspects, four different simulations are presented:

- We compare flow evolutions obtained from CVS using either the threshold ε_0 (run labelled CV-TS) or ε_{it} (CV-DS), respectively. In both cases the security zone is applied.
- The necessity and effect of the security zone is demonstrated by comparing two simulations, one with the security zone (labelled CV-1S) and the other without it (labelled CV-6), starting both the simulations with about the same compression rate. Using the iterative threshold estimation algorithm introduced in section 2.1, we limit the number of iterations in both cases, i.e. one iteration for CV-1S and six iterations for CV-6. Only in the case of the CV-1S run is the security zone added. The number of iterations chosen for these two runs is justified to obtain an approximately identical compression ratio for their resulting initial condition.

The starting point for all these simulations is the initial condition of the DNS run shown in figure 10. After the initial wavelet filtering we obtain the initial conditions for each simulation. The corresponding compression ratios and the percentages of energy and enstrophy conserved are listed in table 1.

The vorticity fields for the CV-TS and the CV-DS simulation run are depicted in figure 11. For the CV-TS run the vorticity field at $\tau = 0$, though it contains most of the energy compared to the unfiltered DNS reference (cf., table 1), looks fragmented and many structures are not completely resolved. At $\tau = 18.2$ we recognize that compared to the reference case the vortices are blurred, deformed and their positions are out of phase. Even their sizes and number differ from the reference. Fine-scale structures are not sufficiently resolved, which is quantified by the spectrum plot in figure 12 for $\tau = 18.2$. Starting at $k = 10$ the spectrum for CV-TS drops below the reference DNS, indicating non-resolved fine structures. The global enstrophy evolution plot exhibits an increasing difference, compared to DNS. Representing with its initial condition 96.2% of the reference's enstrophy, only 88% of enstrophy are conserved for the final vorticity field. These effects are due to the high compression, starting at $\tau = 0$ with a ratio of 2.2% (cf., table 1). The relative compression ratio is shown in figure 12. Furthermore, a comparison of the PDF of the vorticity at $\tau = 18.2$ illustrates significant differences for large vorticity values. We can conclude that the compression resulting from the CV-TS run obviously is too high to reproduce the reference flow accurately with all structures resolved.

Comparing the vorticity fields of the CV-DS (figure 11) and DNS (figure 10) runs by eye no difference can be detected. The plots for the total enstrophy evolution, the PDFs of vorticity, and the energy spectra yield the same result. This high degree of conformity becomes obvious considering the compression, coming along with CV-DS (cf., figure 11). The filtered initial vorticity field is compressed to only 46.9% of degrees of freedom. In addition, the relative compression ratio evolution plot in figure 12 illustrates a global increase to 53.3%, i.e. more than 50% of the degrees of freedom are retained.

As a result from the CV-DS and CV-TS simulation runs, we propose for the practical application of CVS filtering in numerical turbulent flow simulations a modification of the threshold

$$\tau = 0 \qquad\qquad\qquad\qquad \tau = 18.2$$
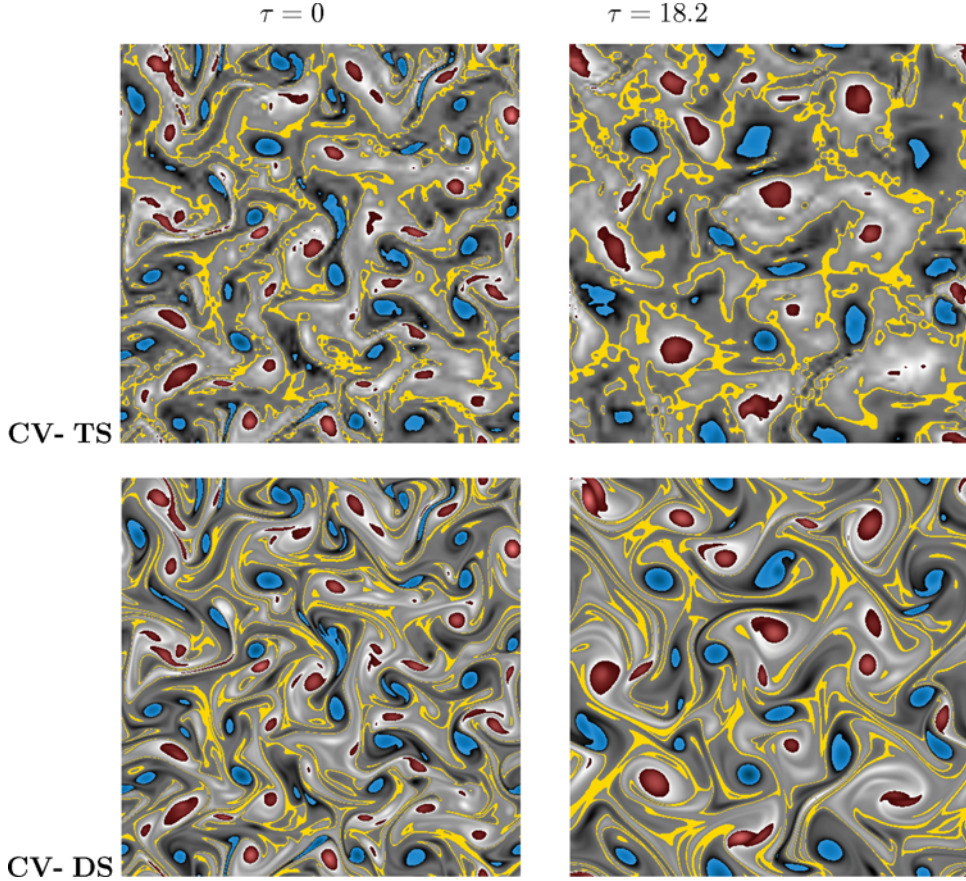
Figure 11.   Vorticity at $\tau = 0$ and at $\tau = 18.2$ of the simulation CV-TS using an estimated threshold ε_0 (top), and CV-DS based on the iteratively evaluated Donoho threshold ε_{it} (bottom). The security zone is applied for both runs. For the colour palette, see figure 10.

estimation algorithm. Instead of using one of the presented extremes, i.e. a threshold based on the total vorticity's variance or the threshold obtained from a converging iteration process, the threshold should be determined by the known iterative threshold estimation procedure performing only a small fixed number of iterations. The number of iterations can be well adjusted to the desired compression and properties to conserve the energy of the particular physical problem. With the following CV-1S run we demonstrate that for the considered two-dimensional flow already one iteration step for the threshold estimation yields a satisfactory flow reproduction in accordance with an acceptable compression.

   The vorticity fields of the CV-1S and the CV-6 runs are depicted in figure 13. Run CV-1S starts with an initial condition reproducing the reference (cf., figure 10) slightly fragmented, but globally no vortices are missing and even finer structures as filaments can be found in the filtered field. At $\tau = 18.2$ the vortices appear a little mutated in shape and some smaller vortices as well as small scale filaments are missing, compared to the reference. However, the vortices number and their positions in space confirm quite well the reference case. Certainly, compared to the highly compressed CV-TS run (see above), the flow field for both time steps is better reproduced in the CV-1S case. The total enstrophy for this run differs not very much from the reference (cf., figure14). Containing 99.4% of the enstrophy of the reference at the
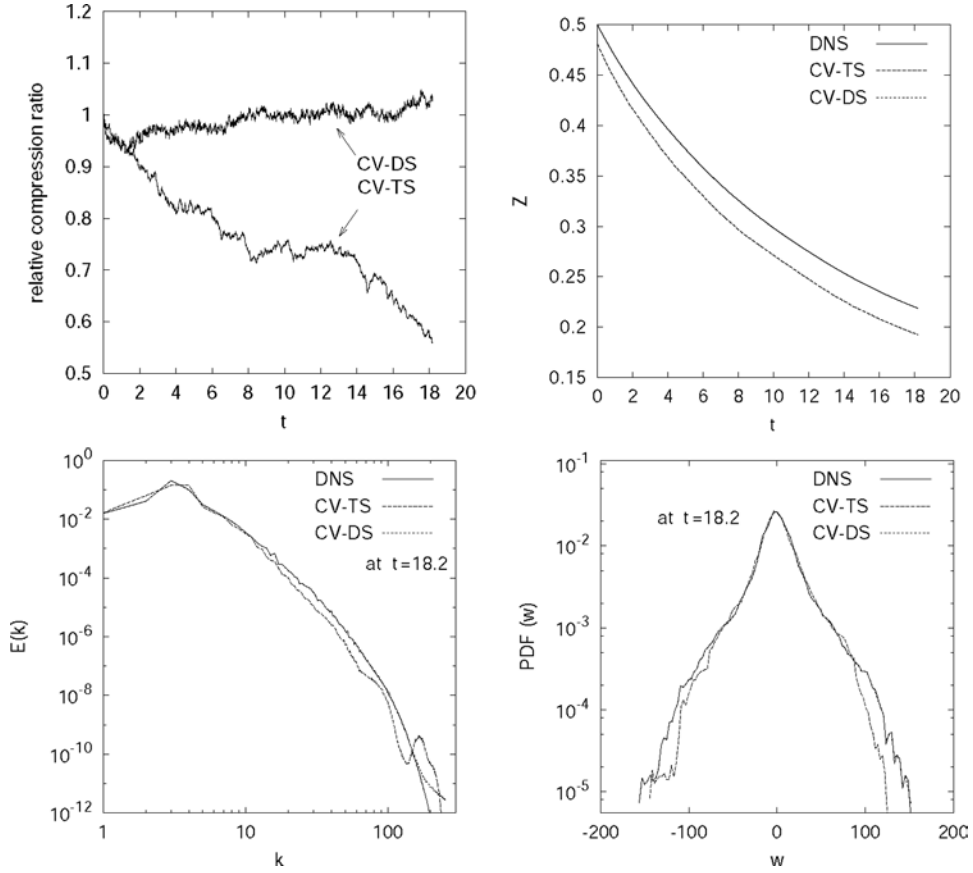
Figure 12.   Comparison between CV-TS, CV-DS and DNS. Top-left: relative compression ratio, i.e. compression normalized by the initial compression at $\tau = 0$. Top-right: total enstrophy evolution. Bottom-left: energy spectra at $\tau = 18.2$. Bottom-right: vorticity PDFs at $\tau = 18.2$. In some plots only two curves can be recognized since in this case DNS and CV-DS are almost identical.

beginning, a small decrease to 97.6% at the end of the simulation is found. Simultaneously, the compression ratio decays from 6.7% to about 5.1% during the evolution. The spectra of CV-1S and DNS at $\tau = 18.2$ are almost identical. Solely at medium wave numbers ($\sim k > 50$) the CV-1S spectrum slips distinctly under the reference, indicating the lack of corresponding fine-scale structures. Finally, the PDF of the vorticity for CV-1S shows no significant deviation from the reference, i.e. the final vorticity field is statistically well reproduced. In summary we can conclude that the major reference dynamical flow information is conserved well in this filtered simulation run. The proposed threshold is affirmed to be a reasonable choice.

The CV-6 run starts with an initial compression ratio of 7%, being only slightly larger than in the CV-1S case. Because no security zone is added in CV-6, the whole set of selected wavelet coefficients yielding the coherent vorticity field represents coherent structures. The CV-1S initial condition is represented by about the same number of wavelet coefficients. But it must be kept in mind, in contrast to CV-6 only a portion of these coefficients represent coherent structures—the rest are only neighbours of coherent structures in wavelet space, chosen to be a part of the coherent vorticity ω_C to account for the flow evolution in scale and space. The CV-6 initial condition looks more similar to the reference's initial condition than the one of
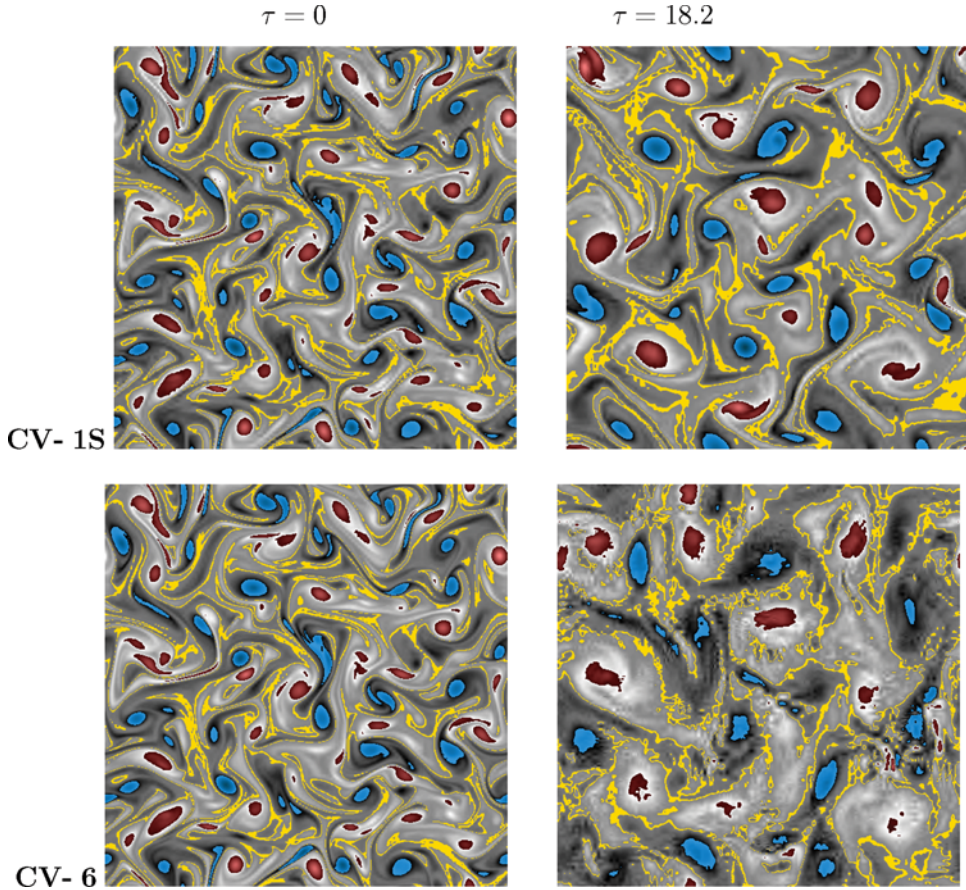
Figure 13.   Vorticity at $\tau = 0$ and at $\tau = 18.2$ of simulation runs CV-1S using a Donoho-based threshold with one iteration plus the security zone, and CV-6 using six iterations without the security zone. For the colour palette, see figure 10.

the CV-1S run (cf., figure 13). But the obvious advantage turns into a disadvantage as soon as the simulation is started and dynamics shall evolve within the selected basis. Because of the lack of 'space' for the solution to evolve within, the effect described in section 3.3 and illustrated in figure 8 for a too small basis takes place: within each time step some dynamically relevant information e.g., structures of non-negligible energy partly leave the integration basis and therefore they are cut off. As a consequence the dynamics of the considered flow are successively destroyed, resulting for the CV-6 in a heavily fragmented vorticity field at the end of the simulation, shown in figure 13. Only the positions of the largest vortices roughly fit the DNS reference. It is not possible to assign smaller vortices to vortices in the reference flow. They are completely out of phase and their number does not correspond to the reference.

Taking into account that CVS filtering is effective in extracting coherent structures from a single flow field, the CV-6 compression ratio decay (cf., figure 14) indicates a fast reduction of the coherent structure quantity. Furthermore, the monotonous decay of the compression ratio exhibits that in the case of a missing security zone the simulation is not able to track coherent structures in the reduced integration basis in scale and space. The steeper decay of the total enstrophy, the energy spectrum and the PDF describing vorticity fields being very different from the DNS or the CV-1S run are subsequent results of the loss of dynamics in the CV-6 run.
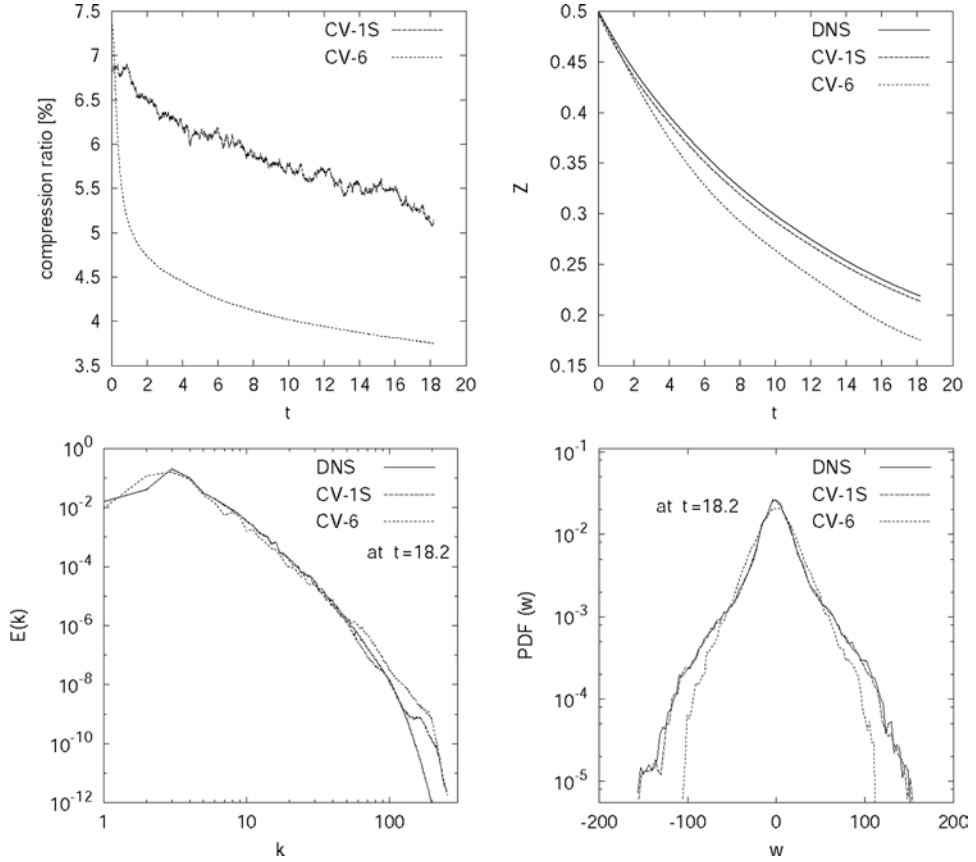
Figure 14. Comparison of CV-1S, CV-6 and DNS. Top-left: compression ratio evolution. Top-right: total enstrophy evolution. Bottom-left: energy spectra at $\tau = 18.2$. Bottom-right: PDF of vorticity at $\tau = 18.2$.

There are two main results from this consideration of the CV-1S and CV-6 simulations. First, for the application to simulations of two-dimensional turbulent flows we proposed a CVS filtering based on the iterative threshold estimation process performing only one iteration. Applied with an additional security zone this choice was found to be a good compromise between high compression and flow reproduction comparable to DNS. The respective extent of information loss that is acceptable for any application has to be decided in each individual case, and it can be controlled by the number of iterations for the threshold estimation and the size of the security zone. Second, the security zone concept was shown to be a reliable way to track the evolution of the flow dynamics in both space and scale. In comparison of the CV-1S and CV-6 runs it was shown that the attachment of the security zone is more important than capturing a maximum of coherent structures by a small threshold.

Results for the CVS $O(\varepsilon)$ model

In the following we present results for the $O(\varepsilon)$ model equations (13) and (14) using three different thresholds, ε_0, ε_1 and ε_{it}, i.e. a threshold based on the variance of the total vorticity, a threshold computed with the iterative algorithm with one iteration only and a threshold computed with the iterative algorithm until convergence.

Table 2. Relative norms of the nonlinear terms with respect to $(\vec{v}_C \cdot \nabla \omega_C)_C$ using different thresholds ε. The values are averaged in time over 20τ.

Term	ε_0	ε_1	ε_{it}
$(\vec{v}_C \cdot \nabla \omega_C)_C$	1	1	1
$(\vec{v}_C \cdot \nabla \omega_C)_I$	7.69×10^{-1}	5.50×10^{-1}	9.51×10^{-2}
$(\vec{v}_C \cdot \nabla \omega_I)_C$	4.59×10^{-1}	2.97×10^{-1}	6.37×10^{-2}
$(\vec{v}_C \cdot \nabla \omega_I)_I$	9.47×10^{-1}	5.34×10^{-1}	8.22×10^{-2}
$(\vec{v}_I \cdot \nabla \omega_C)_C$	7.93×10^{-2}	7.78×10^{-3}	3.29×10^{-4}
$(\vec{v}_I \cdot \nabla \omega_C)_I$	6.25×10^{-2}	9.99×10^{-3}	2.81×10^{-4}
$(\vec{v}_I \cdot \nabla \omega_I)_C$	3.03×10^{-2}	1.40×10^{-3}	1.69×10^{-5}
$(\vec{v}_I \cdot \nabla \omega_I)_I$	6.95×10^{-2}	3.77×10^{-3}	2.25×10^{-5}

To assess the magnitude of the different terms we first perform three DNS for the different thresholds by integrating the equations for ω_C and ω_I (9), (10) without neglecting any terms. For a period of 20τ we compute the norms of all nonlinear terms in both equations. The time average of the relative norms $|| \cdot ||/||(\vec{v}_C \cdot \nabla \omega_C)_C||$ is summarized in table 2. They illustrate the importance of the different terms with respect to the most important one, $(\vec{v}_C \cdot \nabla \omega_C)_C$. For the iterative threshold ε_{it} we can identify three orders of magnitude, i.e. a term of $O(1)$ corresponding to $(\vec{v}_C \cdot \nabla \omega_C)_C$, three terms of $O(\varepsilon)$ corresponding to terms with $\vec{v}_C$ and four terms of $O(\varepsilon^2)$ corresponding to terms with $\vec{v}_I$. This confirms the presented estimation in section 3.1. However, for the thresholds ε_0 and ε_1 we observe that the first three terms with $\vec{v}_C$ cannot be considered as $O(\varepsilon)$ but are $O(1)$ terms. For all cases table 2 also shows that the Leonard stress term, $(\vec{v}_C \cdot \nabla \omega_C)_I = \vec{v}_C \cdot \nabla \omega_C - (\vec{v}_C \cdot \nabla \omega_C)_C$, has the same order of magnitude as the cross terms with $\vec{v}_C$.

Concerning the dependence of the relative norms on the choice of the threshold we observe that for the largest threshold, i.e. ε_0, the magnitude of the $O(\varepsilon^2)$ terms is two orders of magnitude smaller than the norm of $(\vec{v}_C \cdot \nabla \omega_C)_C$, while for small thresholds, i.e. ε_{it}, there is a difference of four orders of magnitude. This motivates the integration of the reduced $O(\varepsilon)$ model equations, where these terms are neglected, to check their actual influence on the dynamics of the flow.

We performed three simulations, integrating the $O(\varepsilon)$ model equations (13), (14) using three different thresholds. The total flow is then reconstructed from the coherent and incoherent flow using equations (8). In figure 15 we show the relative differences of the energy and enstrophy evolution, i.e. $(E(\tau) - E_{DNS}(\tau))/E_{DNS}(\tau)$ and $(Z(\tau) - Z_{DNS}(\tau))/Z_{DNS}(\tau)$, with respect to the DNS reference run. For the CVS $O(\varepsilon)$ simulation with ε_0 we observe that for both quantities
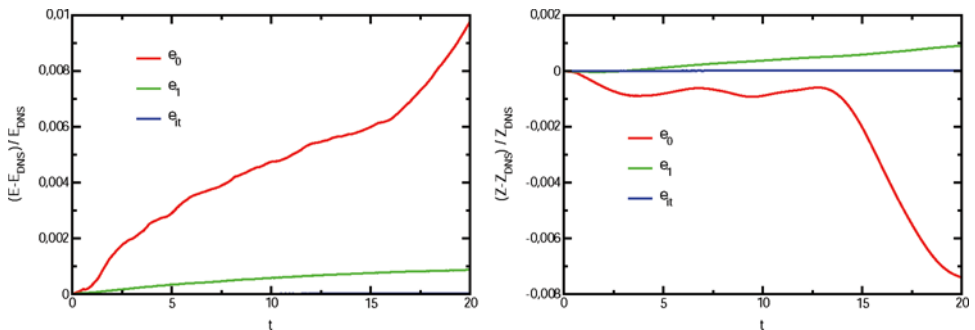
Figure 15. Evolution of energy (left) and enstrophy (right) using the CVS $O(\varepsilon)$ model. Note that for both quantities the relative differences with respect to the DNS results are plotted.

the differences are less than 1% at the end of the run. Compared to the CV-TS run in section 4.2, where the influence of ω_I was simply neglected, we found a difference of 1.8% for the energy and 12% for the enstrophy.

For the CVS $O(\varepsilon)$ simulation with ε_1 the differences of energy and enstrophy with respect to the DNS remain smaller than 0.1%, while for the CVS $O(1)$ simulation (run CV-1S) with ε_1 we found differences of 0.2% for the energy and of 3.9% for the enstrophy (cf. section 4.2). This shows that modelling the influence of ω_I improves the precision of CVS. Note that the CVS $O(\varepsilon)$ simulation with ε_{it} almost perfectly reproduces the DNS results.

5. Conclusion

In this paper we presented CVS of homogeneous isotropic two-dimensional turbulence. CVS is a new method for the simulation of turbulent flows and lies between DNS and LES. The model equations are based on the wavelet filtered Navier–Stokes equations. The time evolution of the coherent vortices is computed deterministically while the influence of the incoherent background noise is either neglected or modelled.

We presented the extraction of dynamically relevant coherent vortices out of turbulent flows. The method is based on a wavelet decomposition of the vorticity, a subsequent thresholding of the wavelet coefficients and a reconstruction of the coherent flow from those coefficients being larger than a given threshold. We compared two different choices of thresholds and showed that thus a flow realization can be split into coherent vortices and quasi-Gaussian white noise. The coherent vortices correspond to few wavelet coefficients only, which contain most of the energy and enstrophy. The computational complexity of the coherent vortex extraction algorithm is of $\mathcal{O}(N)$, where N denotes the number of grid points. Note that parallel implementations of fast wavelet transforms are available, see e.g. [16].

We then derived model equations for CVS by splitting the Navier–Stokes equations written in velocity–vorticity formulation into evolution equations for the coherent and incoherent vorticities. A hierarchy of model equations inspired by the nonlinear Galerkin approach was developed. In the previously presented CVS method [11] there was no modelling of the effect of the discarded coefficients performed. Filtering out the incoherent background at each time step played the role of turbulent dissipation. Using this CVS model we presented different numerical simulations to study the role of the choice of the threshold (iterated or not) and the influence of the security zone. By comparing simulations for the same compression rate with and without the security zone, we found that the security zone plays an essential role to track the flow evolution in space and scale. Furthermore, we showed that depending on the required precision of the simulations one iteration to determine the threshold can be sufficient.

In the new two-equation CVS approach we derived an additional linear evolution equation for the incoherent vorticity to compute the effect of the incoherent background flow whose coefficients have been discarded. We analysed the different terms of the filtered equations. We then performed CVS of homogeneous isotropic turbulence and validated the two-equation model. Compared to the CVS model where the influence of the incoherent flow is discarded we found an improved precision.

The extension of CVS to compute three-dimensional turbulent flows is currently under way; results for a turbulent mixing layer discarding the incoherent vorticity to model turbulent dissipation have been presented in [29]. Future studies will deal with applications which take advantage of the CVS property to preserve locally small-scale activity. Their influence may become important, e.g. for turbulent mixing in reactive flows, where small scales are important for molecular mixing and chemical reactions.

Acknowledgements

References

[1] Azzalini, A., Farge, M. and Schneider, K., 2005, Nonlinear wavelet thresholding: A recursive method to determine the optimal denoising threshold. *Applied Computational Harmonic Analysis*, **18**(2), 177–185.

[2] Canuto, C., Hussaini, M.Y., Quaternioni, A. and Zang, T.A., 1988, *Spectral Methods in Fluid Dynamics* (Berlin: Springer).

[3] Chasnov, J.K., 1997, On the decay of two-dimensional homogeneous turbulence. *Physics of Fluids*, **9**(1), 171–180

[4] Cohen, A., 2000, In P.G. Ciarlet and J.L. Lions (Eds.), *Wavelet Methods in Numerical Analysis*, vol. 7 of *Handbook of Numerical Analysis* (Amsterdam: Elsevier).

[5] Constantin, P. and Foias, C., 1988, *Navier–Stokes Equations* (Chicago: University of Chicago Press).

[6] Daubechies, I., 1992, *Ten Lectures on Wavelets* (Philadelphia: SIAM).

[7] DeVore, R., 1998, Non-linear approximation. *Acta Numerica*, **7**, 51–150.

[8] Donoho, D., 1995, De-noising by soft thresholding. *IEEE Transaction on Information Theory*, **41**, 613–627.

[9] Donoho, D. and Johnstone, I., 1994, Ideal spatial adaptation via wavelet shrinkage. *Biometrika*, **81**, 425–455.

[10] Farge, M., 1992, Wavelet transforms and their applications to turbulence. *Annual Review of Fluid Mechanics*, **24**, 395.

[11] Farge, M., Schneider, K. and Kevlahan, N., 1999, Non-Gaussianity and coherent vortex simulation for two-dimensional turbulence using an adaptive orthonormal wavelet basis. *Physics of Fluids*, **11**(8), 2187–2201.

[12] Farge, M. and Schneider, K., 2001, Coherent vortex simulation (CVS), a semi-deterministic turbulence model using wavelets. *Flow, Turbulence and Combustion*, **66**(4), 393–426.

[13] Farge, M., Pellegrino, G. and Schneider, K., 2001, Coherent vortex extraction in 3D turbulent flows using orthogonal wavelets. *Physical Review Letters*, **87**(5), 45011–45014.

[14] Farge, M., Schneider, K., Pellegrino, G., Wray, A. and Rogallo, B., 2003, Coherent vortex extraction in three-dimensional homogeneous turbulence: Comparison between CVS-wavelet and POD-Fourier decompositions. *Physics of Fluids*, **15**(10), 2886–2896.

[15] Fröhlich, J. and Schneider, K., 1997, An adaptive wavelet–vaguelette algorithm for the solution of PDEs. *Journal of Computational Physics*, **130**, 174–190.

[16] Goirand, E., Wickerhauser, V. and Farge, M., 1994, A parallel two-dimensional wavelet packet transform and some applications in computing and compression analysis. In B. Joseph and R. Motard (Eds.), *Applications of Wavelets to Chemical Engineering* (Dordrecht: Kluwer), pp. 275–319.

[17] Grossmann, A. and Morlet, J., 1984, Decomposition of Hardy functions into square integrable wavelets of constant shape. *SIAM Journal on Mathematical Analysis*, **15**, 723–736.

[18] Goldstein, D.E. and Vasilyev, O.V., 2004, Stochastic coherent adaptive large eddy simulation method. *Physics of Fluids*, **16**(7), 2497–2512.

[19] Margolin, L., Titi, E. and Wynne, S., 2003, The postprocessing Galerkin and nonlinear Galerkin methods – a truncation analysis point of view. *SIAM Journal on Numerical Analysis*, **41**(2), 695–714.

[20] Mc Williams, J.C., 1984, The emergence of isolated coherent vortices in turbulent flows. *Journal of Fluid Mechanics*, **146**, 21–43.

[21] Meneveau, C., 1991, Analysis of turbulence in the orthonormal wavelet representation. *Journal of Fluid Mechanics*, **232**, 469–520.

[22] Mrázek, P., Weickert, J. and Steidl, G., 2003, Correspondences between wavelet shrinkage and nonlinear diffusion. In L.D. Griffin and M. Lillholm (Eds.), *Scale-Space 2003*, LNCS vol. 2695 (Berlin: Springer), pp. 101–116.

[23] Perona, P. and Malik, J., 1990, Scale space and edge detection using anisotropic diffusion. *IEEE Transactions on Pattern Analysis and Machine Intelligence*, **12**, 629–639.

[24] Schneider, K., Kevlahan, N. and Farge, M., 1997, Comparison of an adaptive wavelet method and nonlinearly filtered pseudo-spectral methods for two-dimensional turbulence. *Theoretical and Computational Fluid Dynamics*, **9**(3/4), 191–206.

[25] Schneider, K. and Farge, M., 1998, Wavelet approach for modeling and computing turbulence. *Lecture Series 1998–05 Advances in Turbulence Modelling*, Bruxelles: von Karman Institute for Fluid Dynamics, 132 pages.

[26] Schneider, K. and Farge, M., 2000, Numerical simulation of temporally growing mixing layer in an adaptive wavelet basis. *Comptes Rendus de l'Academie des Sciences, Paris Série II b*, **328**, 263–269.

[27] Schneider, K. and Farge, M., 2002, Adaptive wavelet simulation of a flow around an impulsively started cylinder using penalisation. *Applied Computational Harmonic Analysis*, **12**, 374–380.

[28] Schneider, K., Farge, M. and Kevlahan, N., 2004, Spatial intermittency in two-dimensional turbulence: a wavelet approach. In N. Tongring and R.C. Penner (Eds.), *Woods Hole Mathematics, Perspectives in Mathematics and Physics*, Vol. 34 (Singapore: World Scientific), pp. 302–328.

[29] Schneider, K., Farge, M., Pellegrino, G. and Rogers, M., 2005, Coherent vortex simulation of 3D turbulent mixing layers using orthogonal wavelets. *Journal of Fluid Mechanics*, **534**, 39–66.